ACSNANO

www.acsnano.org

ARTICLE

Wide-Range Size Fractionation of Graphene Oxide by Flow Field-Flow Fractionation

Hee Jae Choi,[⊥] Myoungjae Ko,[⊥] In Ho Kim, Hayoung Yu, Jin Yong Kim, Taeyeong Yun, Joon Seon Yang, Geon Gug Yang, Hyeon Su Jeong, Myeong Hee Moon,* and Sang Ouk Kim*

Cite This: *ACS Nano* 2022, 16, 9172–9182

Read Online

ACCESS | Metrics & More | Article Recommendations | Supporting Information

ABSTRACT: **Many interesting properties of 2D materials and their assembled structures are strongly dependent on the lateral size and size distribution of 2D materials. Accordingly, effective size separation of polydisperse 2D sheets is critical for desirable applications. Here, we introduce flow field-flow fractionation (FlFFF) for a wide-range size fractionation of graphene oxide (GO) up to 100 μm. Two different separation mechanisms are identified for FlFFF, including normal mode and steric/hyperlayer mode, to size fractionate wide size-distributed GOs while employing a crossflow field for either diffusion or size-controlled migration of GO. Obviously, the 2D GO sheet reveals size separation behavior distinctive from typical spherical particles arising from its innate planar geometry. We also investigate 2D sheet size-dependent mechanical and electrical properties of three different graphene fibers produced from size-fractionated GOs. This FlFFF-based size selection methodology can be used as a generic approach for effective wide-range size separation for 2D materials, including rGO, TMDs, and MXene.**

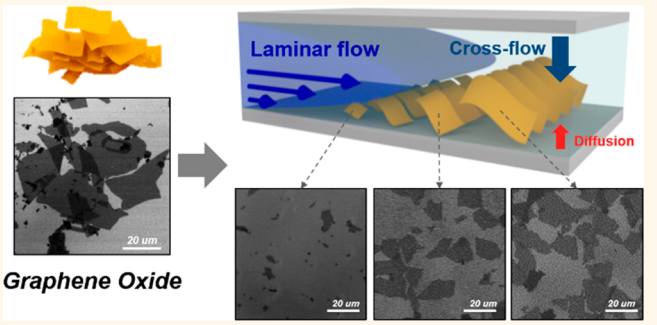

KEYWORDS: *graphene oxide, size fractionation, flow field-flow fractionation, graphene fiber, 2D materials*

Graphene oxide (GO), a typical chemically modified graphene, is emerging as a two-dimensional (2D) material with soft-matter-like characteristics, including high solvent dispersibility, biocompatibility, and dense surface chemical functionality.[1−4] Such uncommon features allow GO to be exploited for a variety of application areas, such as conductive fibers, 3D printable ink, membranes, catalysts, sensors, energy storage devices, bioscaffolds, and antipollutants.[5−12] Notably, our discovery of the liquid crystalline (LC) phase formation of GO in 2009 led to research on highly ordered functional material fabrication.[13] Moreover, a fully exfoliated monolayer GO in the LC state offers an ideal precursor for the large-scale production of minimal layers (three to five layers) of stacked graphene platelets, which are very useful in the recent commercial market.[14]

In general, GO inevitably has a broad size distribution due to its predominant synthetic pathway via random chemical exfoliation of graphite.[15−18] As the typical material properties of GO strongly depend on the lateral size, the size selection of GO is a crucial requirement for the desired material applications. For instance, large-size GO with a relatively lower edge/basal plane ratio is useful for a graphene-based structure with strong mechanical strength mediated by intimate interlayer interaction (i.e., $\pi-\pi$ interactions) as well as high electrical/thermal conductivity along the large layer plane.[19−21] In contrast, small-size GO bears an advantage in the solution process due to its higher solvent dispersibility and good antibacterial effect with a dense population of surface functional groups.[22−24] To date, several size fractionation strategies have been introduced for GO, including LC biphasic size separation, directional freezing, track-etched membrane, pH-assisted sedimentation, and density gradient ultracentrifugal separation.[11,12,25−27] Unfortunately, most of those previous methods revealed specific size ranges for effective selection. Precise size selection over a broad range of size distribution still remains a challenging issue.

Field-flow fractionation (FFF) is a laminar flow-based separation method relying on the subtle control of a size-dependent diffusion coefficient under an external field (e.g., flow, thermal, sedimentation, and electrical field) according to

Received: February 10, 2022
Accepted: June 2, 2022
Published: June 9, 2022

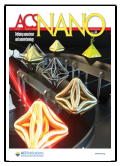

https://doi.org/10.1021/acsnano.2c01402
ACS Nano 2022, 16, 9172−9182

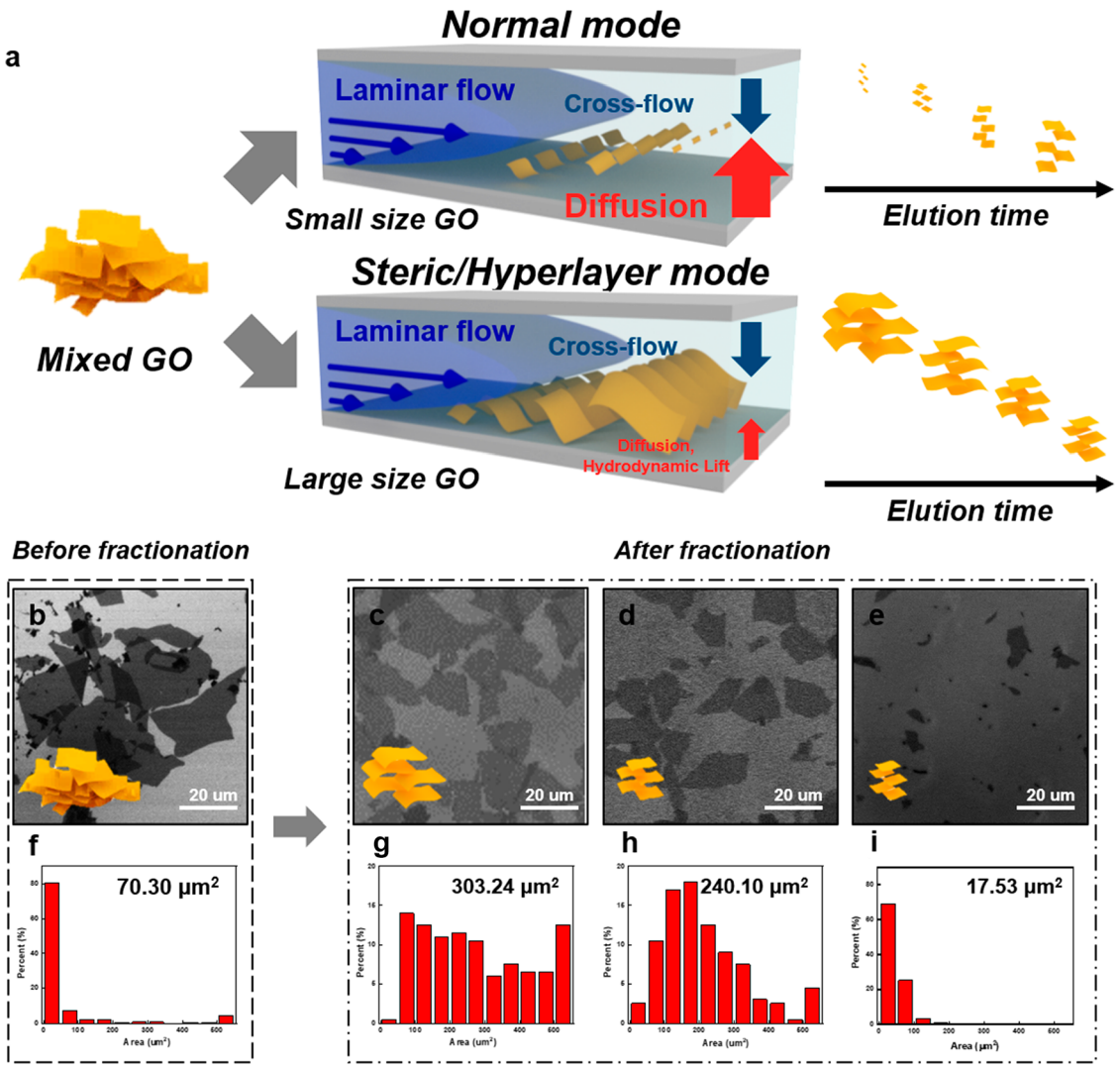

Figure 1. Size fractionation of GO via FlFFF. (a) Schematic illustration of GO size fractionation GO via flow field-flow fractionation. The retention of GO is controlled by the interaction between the crossflow (blue arrow) from moving across the channel (from upper channel wall to the bottom (accumulation) wall) and diffusion or hydrodynamic lift forces against the accumulation wall (red arrow). The small-size GO is strongly affected by diffusion force. On the contrary, diffusion force is relatively less dominant for large-size GOs. (b) SEM image and (f) size distribution of MGO before size fractionation (dashed line). SEM images of representative MGO fractions: (c) MGO F1, (d) MGO F3, and (e) MGO F7. Size distributions of representative MGO fractions: (g) MGO F1, (h) MGO F3, (i) MGO F7 (dash-dotted line).

the sensitive properties of a target material.[28] Among them, flow FFF (FlFFF) is a flow field-induced size-fractionating subtechnique generally used for latexes, metal particles, biomolecules, or polymers under the two different flow streams: migration flow and crossflow. While the migration flow carries a target sample material along the separation channel toward a detector, the crossflow moving across the channel cross-section forces sample components toward the channel (accumulation) wall, resulting in the control of particle retention.[29,30] This retention effect affected by the relative rates of crossflow (or external field) and migration flow (or channel flow) can also be expressed by the Stokes' equation. Additionally, the composition, ionic strength, and pH of the carrier solution affect the electrical double layer of the sample in FlFFF separation.[31] Consequently, various factors such as the channel void volume, crossflow rate, migration flow rate, viscosity of the solution, and Stokes' diameter of analyte should be considered for an optimum size selection condition.[32] To the best of our knowledge, GO size fractionation based on the FlFFF system has not been reported thus far. It is noteworthy that FlFFF has distinctive advantages for the size fractionation of GO. FlFFF is a generic environmentally benign method, theoretically known to separate a wide range of target materials from 1 nm to 100 μm, which sufficiently covers the innate broad size distribution of typical GO samples (Figure S2, Supporting Information).[33] In addition, mild laminar flow inside the separation channel does not damage GO upon a separation process.

In this work, we introduce a wide-range size fractionation of 2D GO by means of FlFFF and its influence on the physical/electrical properties, particularly in the form of graphene LC fiber structure. For 2D flake GO, the normal mode region, mainly governed by diffusion force, is found to be up to 2 μm, which is greater than the typical 1 μm for conventional spherical particles. In contrast, GO platelets larger than 3 to 4 μm could be separated via a steric/hyperlayer mode.

https://doi.org/10.1021/acsnano.2c01402
ACS Nano 2022, 16, 9172−9182

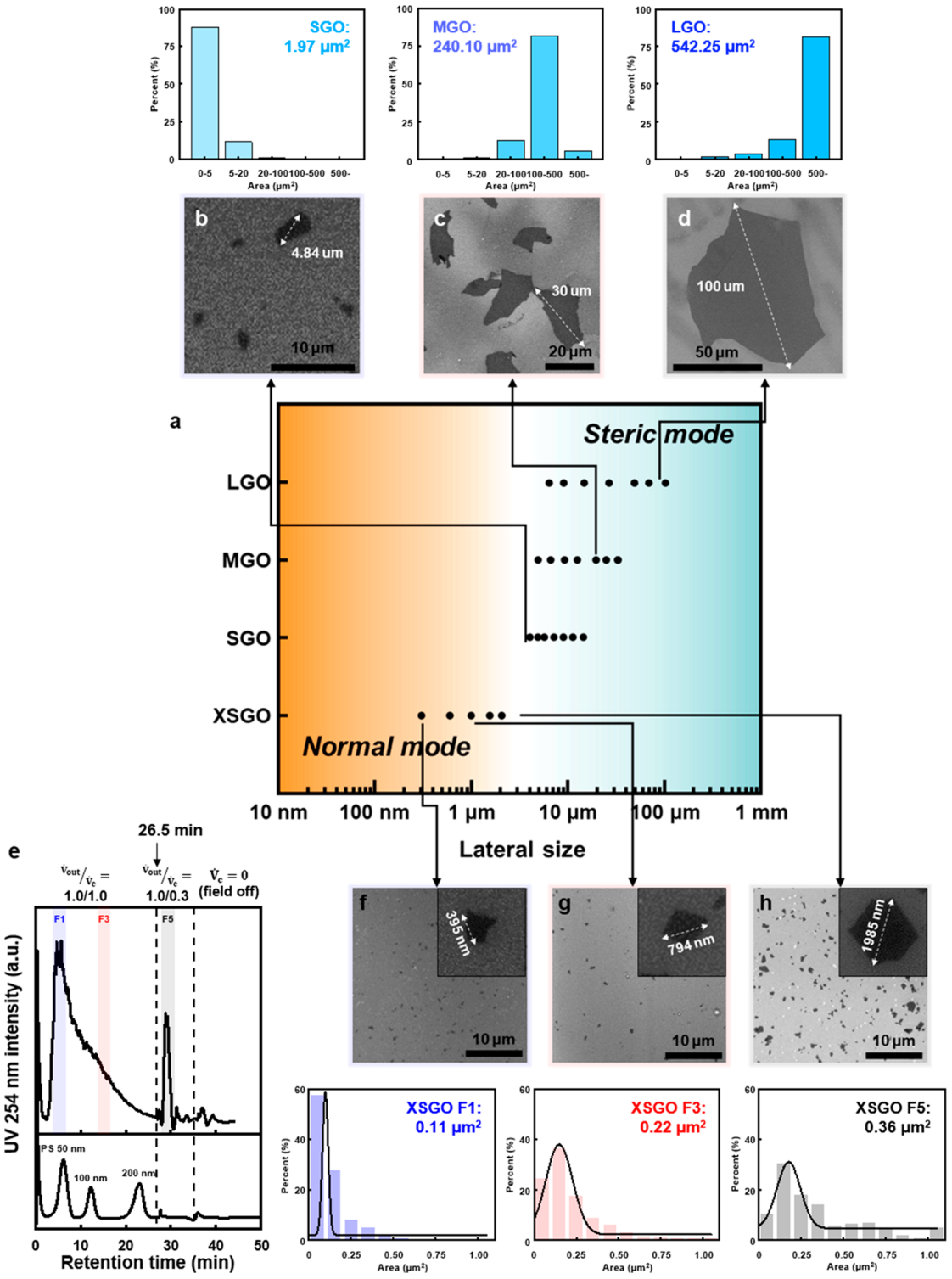

Figure 2. Wide range size fractionation of four different GOs by FlFFF. (a) Size fractionation results of the four different GOs (XSGO, SGO, MGO, and LGO). Along with the lateral size of GO, different size fractionation modes were applied. Normal mode was only applied for the XSGO. Steric/hyperlayer mode was applied for SGO, MGO, and LGO. Representative SEM images and size distributions of (b) F1 in SGO, (c) F3 in MGO, and (d) F2 in LGO. (e) Size fractionation result of XSGO (upper part) and size fractionation result of the three different sizes of PS beads (PS 50, 100, and 200 nm, bottom part). (f–h) SEM images and size distributions of F1, 3, and 5 in XSGO and its size distribution.

RESULTS AND DISCUSSION

Stable aqueous dispersions of monolayer exfoliated GO samples were synthesized by our modified hummers method and subsequent purification.[13] The random chemical exfoliation yields GO platelets with a broad range of size distribution, which is well consistent with the inherent separable range of FlFFF.[34,35] Figure 1a schematically illustrates the size fractionation of as-synthesized GO with FlFFF. While aqueous dispersed GOs were injected into an FlFFF channel, the broad

https://doi.org/10.1021/acsnano.2c01402
ACS Nano 2022, 16, 9172–9182

size distributed GOs were separated with different elution times depending on their size in the channel. The migration flow (laminar flow) carries GOs to the end of the channel.

The separation mode of FlFFF can be classified into two different categories, including normal mode and steric/hyperlayer mode. For small-size GOs, Brownian diffusion tends to induce a uniform spatial distribution inside the separation channel against the bottom (accumulation) wall. By adjusting the balances between Brownian diffusion force and crossflow rate, small GOs are sufficiently located away from the bottom wall of the channel toward the fast streamlines of parabolic laminar flow. In this regard, particles having submicron sizes can be separated from small to large sizes with elution time, which is generally called a normal mode. By contrast, Brownian diffusion is relatively less dominant for large-size GOs. Under the negligible diffusion effect, the center of mass for the large-size GOs should be away from the bottom (accumulation) wall simply due to the hydrodynamic lift forces dependent on particle size and shape factor, such that large-size GOs are more lifted toward the center of the laminar flow to determine the rapid elution order (i.e., larger sized GOs elute earlier than smaller sized GOs). This mechanism generally called a steric/hyperlayer mode is observed for the spherical particles over 1 μm sizes.[31,36,37] It is noteworthy that along with the combination of these two different mechanistic modes, almost the entire size range of GO can be separated by FlFFF, which could be verified by the effective separation of four different representative GO samples with different average sizes, including extra small GO (XSGO), small GO (SGO), medium GO (MGO), and large GO (LGO). Using the different graphite sources, LGO and MGO were synthesized by a modified Hummer's method.[13,15] Size and distribution of MGO and LGO are summarized in Figure S3. The SGO and XSGO were synthesized by bath-sonication and tip-sonication of MGO.

The lateral size of the four different GO samples was characterized by scanning electron microscopy (SEM), and the thickness of the GO samples was confirmed by atomic force microscopy (AFM). GO platelets were deposited and dried at SiO_2 surfaces for the computer-aided statistical analysis of their lateral sizes. As confirmed by AFM analysis, all of the samples show monolayer dominant characteristics in their thickness (<1 nm) (Figure S4). Figure 1b–i presents the size and size distribution change before and after the size separation of MGO by FlFFF. The as-synthesized MGO sample shows a typical broad distribution, including a few microns to hundreds of microns in the lateral sizes (Figure 1b,f). Figure 1c–e presents the SEM images of three representative fractions from MGO (MGO F1: fraction 1, MGO F3: fraction 3, and MGO F7: fraction 7). Figure 1g–i shows the statistical distributions of GO platelet lateral areas for each fraction. Noticeably, the full-size range of MGO could be successfully separated by the steric/hyperlayer mode. After the short initial void peak (~0.6 min.), the elution level of MGO is sharply increased and then gradually decreases with elution time. In particular, large-size GOs over 100 μm^2 are frequently observed in F1–3 but rarely found near the late fractions (F4–7) along with the fractogram of the MGO sample (Figure S6). This implies that the size fractionation of GO by FlFFF is very effective between large-size and small-size GOs.

When a GO sample is separated by FlFFF, the recovery of injected sample is about 78.4%. This is because some of GOs may remain at the bottom wall of channel or some are spread during elution by dilution. The recovery of the sample can be tuned by controlling the cross-flow-field strength.[38,39] Additionally, the recovery and resolution of GO can be adjusted by changing the carrier solution or channel membrane. Elution behaviors of the as-synthesized MGO as well as the information on each fraction from FlFFF can be summarized along with the comparison to those of reference spherical polystyrene (PS) latex standard samples (2, 6, 10, and 20 μm) obtained in the same experimental conditions ($\dot{V}_{out}/\dot{V}_c$ = 1.74/0.09 mL/min, $\dot{V}_{out}$: migration flow, $\dot{V}_c$: crossflow). From a direct comparison of the elution behaviors, the same elution time leads to the much larger average diameter of the 2D GO platelet compared to the spherical PS standard. A calibration curve of MGO is established as log t_r (min) = −1.48 log d (μm) + 2.04, where 1.48 is the diameter selectivity (S_d) and 2.04 is the extrapolated logarithmic retention time (log t_{r1}) for 1 μm particles. For the spherical PS latex, a calibration curve is established as log t_r (min) = −0.85 log d (μm) + 1.39. Based on the standard calibration curve, the retention time of spheres corresponding to the average disc diameter of GO sheets can be estimated for each fraction. The overall retention times for MGO F1 to MGO F7 are much shorter than those of spherical particles due to the increased hydrodynamic lift forces for flat GO sheets.

To clarify the size-separation behavior between the normal mode and steric/hyperlayer mode for 2D GO, separation results for the four different GO samples are summarized in Figure 2a. Each colored region indicates the separation mode for GO size, and the discreteness region represents the GO diameter of the normal to steric transition. The data points correspond to the mean value for the largest lateral dimension of each GO sheet. The average size and distribution of GO can be tuned by simply changing of acquisition time. Among all samples, only XSGO was separated by the normal mode. Figure 2e compares the retention behaviors of the XSGO and the submicron-sized PS standards (50, 100, and 200 nm). The initial separation condition was changed from $\dot{V}_{out}/\dot{V}_c$ = 1.0/1.0 mL/min (initial condition) to $\dot{V}_{out}/\dot{V}_c$ = 1.0/0.3 mL/min to release the large GO sheets trapped within the channel during the experiment (around 26.5 min in Figure 2e). Accordingly, most of the trapped large GOs (F5 in XSGO) could be eluted shortly. In addition, the average area of each fraction is steadily increased with the fraction number (XSGO F1:0.11 μm^2, XSGO F3:0.22 μm^2, XSGO F5:0.36 μm^2 in Figure S7).

Figure 2f–h exhibits the representative SEM images and the corresponding size distributions of XSGO for the three collected fractions. For instance, 400 nm sized GOs are eluted at 6–7 min, which matches with the elution time for ~50 nm spherical PS particle. The shortening of elution time is more prominent in the normal mode compared to the steric mode, which is principally attributed to the stronger hydrodynamic lift force for the 2D planar geometry. Additionally, the steric-entropic effect of 2D GO also causes the reduction of retention time in the FFF channel by the entropic restriction of disc-shaped particles (see the Methods).[40] In contrast, GO sheets with an average lateral size of over 2 μm were separated by the steric/hyperlayer mode (larger sized GO eluted earlier than smaller sized GO). For SGO, thus, the elution behavior is entirely opposite to XSGO. The last fraction for SGO (SGO F7) has the average diameter around 4 μm (Figure 2b). The FlFFF fractogram of SGO along with the SEM images and size distribution of the seven collected fractions are in Figure S8.

https://doi.org/10.1021/acsnano.2c01402
ACS Nano 2022, 16, 9172–9182

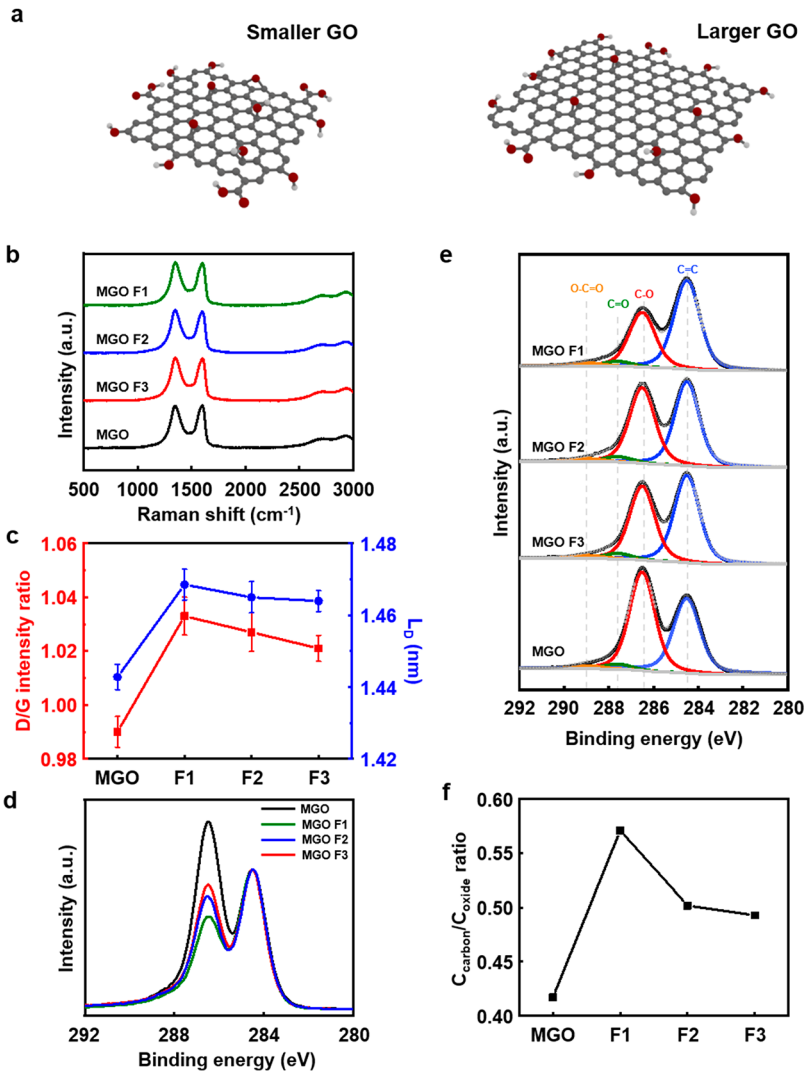

Figure 3. Chemical analysis of GO before and after size fractionation. (a) Schematic illustration of smaller GO (left) and larger GO (right). (b) Raman spectra of MGO, MGO F1, MGO F2, and MGO F3. (c) I_D/I_G intensity ratio and mean distance between two defects of MGO, MGO F1, MGO F2, and MGO F3. (d) Relative intensity of XPS C 1s spectra of MGO, MGO F1, MGO F2, and MGO F3. (e) XPS analysis for chemical compositions of MGO, MGO F1, MGO F2, and MGO F3 at the C 1s region. (e) Carbon to oxide element ratio based on XPS C 1s speaks.

These results suggest that the boundary of separation mechanism between normal mode and streic/hyperlayer mode is approximately 3 μm for GO. Note that the shape factor of the thin GO sheets is a contributing factor in the increase of the hydrodynamic lift force, resulting in the fast elution of large GO sheets. Figure 2c,d summarizes the representative SEM images and statistics for the fractionations from MGO and LGO samples (see Figures S6 and S9 for information for all of the collected fractions of MGO and LGO, respectively). The theoretical limit for the size fractionation by employing FlFFF is generally known to be ~100 μm.[41,42] Interestingly, the 100 μm GO sample could be successfully size-separated by FlFFF. Depending on the flow rate condition and channel thickness, particles larger than 100 μm in diameter can be resolved. However, if the particle size is too large, the height of particle migration at the given channel thickness becomes too high, and the sample components will be swept the channel along the void peak without being retained in the channel.

The precise size selection of GO is advantageous in various research areas, including sensors, energy storage, and wearable devices.[43−45] In the fiber spinning from GO LC, preliminary size selection of GO is highly desirable for the control of final material performances. Usually, large-size GO can make the highly aligned ordered arrangement in the fiber, while small-size GO serve to fill the defects and microvoids within the fiber volume. To verify the effect from size distribution, graphene fibers were spun from aqueous GO LC dispersions with narrow lateral size distributions.[46−48] For the effective fractionation of a large amount of GO sample, we repeated the size fractionation procedure by semipreparative scale FlFFF. The aqueous dispersion of our highly purified GO revealed typical nematic type colloidal LC phase. As reported previously, GO LC formation is strongly affected by the lateral size and the concentration of GO sheets.[21,46] We systematically investigated the effect from GO size on the electrical and physical characteristics of the resultant graphene fibers by employing F1, F2, and F3 from the MGO sample, which has a considerable amount of large-size GO sheets (>100 μm^2).

https://doi.org/10.1021/acsnano.2c01402
ACS Nano 2022, 16, 9172−9182

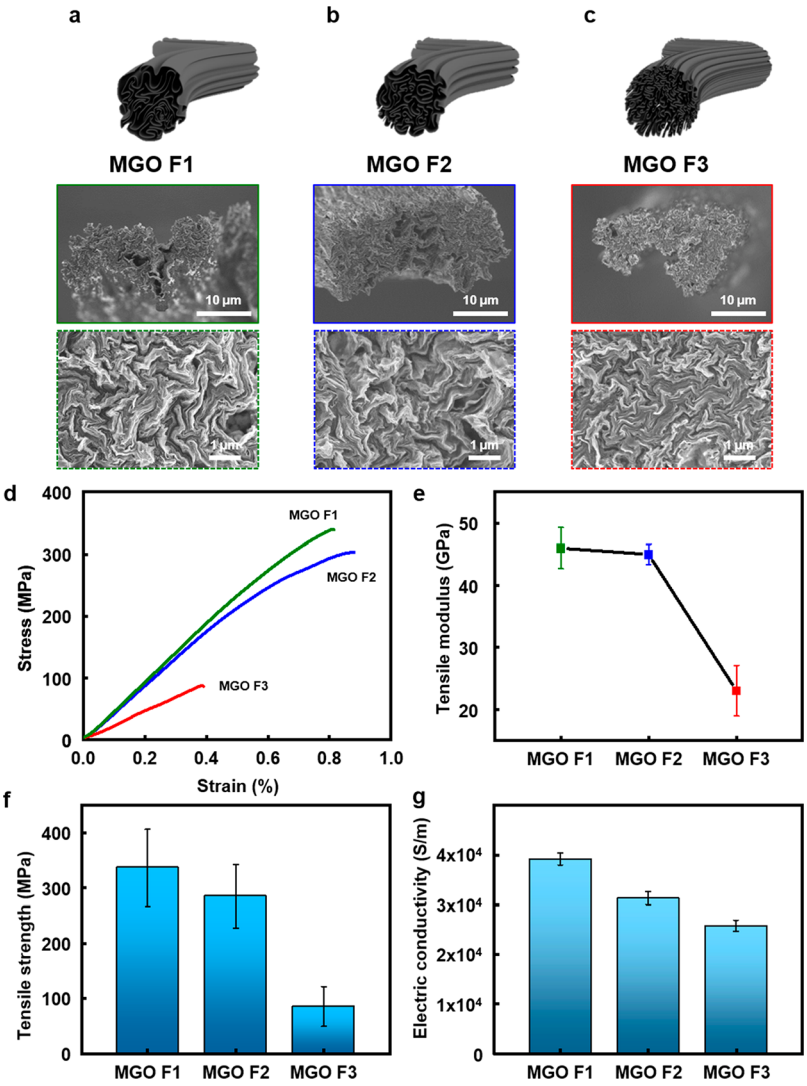

Figure 4. Mechanical and electrical properties of size-fractionated graphene fiber. (a–c) Schematic illustrations and cross-sectional SEM images (solid line) and high-magnification SEM images (dotted line) of thermally reduced graphene fibers: MGO F1, MGO F2, and MGO F3. (d) Stress–strain curves for thermal reduced graphene fibers: MGO F1, MGO F2, and MGO F3. (e) Tensile modulus of fibers, (f) evolution of tensile strength, and (g) electrical conductivities of fibers: MGO F1, MGO F2, and MGO F3.

Upon chemical oxidation and exfoliation of graphite, oxygenated functional groups are known to be more populated at the edge sites of GO rather than its basal plane.[17,49,50] As the edge-to-basal plane ratio of 2D GO generally increases along with the decrease of its lateral size, the mean areal density of hydrophilic functional groups and relevant defect structures is thus higher in small-size GO compared to large-size GO (Figure 3a).[51−53] A large amount of GO sample was successfully obtained, from which careful chemical analyses were conducted to analyze the influences from chemical compositions arising from the average sheet sizes. Raman spectroscopy was used to find a relationship between the intensity ratio of the D to G peak (I_D/I_G) and GO size, which is commonly useful for evaluating the average distance between defects (L_D) in graphene-based materials. The I_D/I_G values for the as-synthesized MGO, MGO F1, MGO F2, and MGO F3 were measured to be 0.993, 1.033, 1.027, and 1.021, respectively.[25,54] As expected, large-size GO revealed a lower defect density than small-size GO. The corresponding L_D values were calculated to be 1.442, 1.468, 1.464, and 1.463, respectively.

A further chemical analysis was performed with X-ray photoelectron spectroscopy (XPS) to compare the C 1s spectra of the size-fractionated GO and as-synthesized MGO (Figure 3d,e). The high-resolution C 1s spectrum of GO exhibits the peaks for C−C bonding at 284.6 eV, C−O bonding at 286.6 eV, C═O bonding at 287.9 eV, and O−C═O bonding at 288.9 eV, respectively.[55,56] Usually, large-size GOs show high C/O ratios. The peak intensity ratio between intact carbon (C−C/C═C) and oxygenated carbon atoms (C−O, C═O, and O−C═O) was considered for the oxidation level of GO, which decreases in the following sequence: as-synthesized MGO > MGO F3 > MGO F2 > MGO F1 (Figure 3d). This verifies that large-size GOs with less functional groups are more populated in the following sequence: MGO F1 > MGO F2 > MGO F3. The C/O ratios of as-synthesized MGO, F1, F2, and F3 were calculated by the deconvolution of C 1s spectra, yielding 0.417, 0.571, 0.502, and 0.493, respectively. Compared to the as-synthesized MGO, F1, F2, and F3 show the higher C/O ratios, revealing a proportional relationship with GO size. These analyses signify that GOs with large lateral sizes were well-separated in the

https://doi.org/10.1021/acsnano.2c01402
ACS Nano 2022, 16, 9172−9182

early stage of separation fractions (MGO F1, MGO F2, and MGO F3).

Graphene fibers were prepared by ambient wet-spinning from size-fractionated MGO LC dispersions (MGO F1, MGO F2, and MGO F3) by employing a homemade syringe pump based wet-spinning equipment. The LC characteristics of MGO aqueous dispersions induce uniaxial alignment of GO sheets during the extrusion from the syringe needle into the coagulation bath to yield highly aligned GO fiber structures. The well-aligned fiber morphology was principally stabilized by the ionic bridge formation among the uniaxial aligned GO sheets, mediated by multivalent cations (Ca^{2+}) dissolved in the coagulation bath. The resultant GO fibers were subsequently heat treated up to 1000 °C under the H_2 atmosphere for the thermal reduction of constituting GO sheets. The mechanical properties of the fibers were characterized by the typical tensile test with a fiber specific sample grip.

Figure 4a–c presents the schematic illustrations and typical SEM images of the fractured morphology of graphene fibers after the tensile test. The cross-sectional morphology is clearly influenced by the average size of the constituting reduced GO (rGO) sheets. While the fibers prepared from the large sizes of GO exhibit relatively rough fractured surfaces with noticeable pull-outs of rGO sheets, small-size GO leads to the simple flat fractured surface. This distinction originates from the size-dependent intersheet interactions and overlap areas among the neighboring rGO sheets.[21,57] Apparently, large-size rGO suffers from severe folding and wrinkling of planar 2D structure to fit into the circular geometry of fiber, yielding more voids and defects in the cross-section. By contrast, small-size rGOs constitute dense, well-packed morphology with less distortion of 2D structure. Nonetheless, small-size rGO results in the relatively weak intersheet interaction among the neighboring rGO sheets due to the intrinsic small sheet-to-sheet contacting area, which causes the typical flat fractured surface of the brittle fracture.[46] In stark contrast, large rGO sheets facilitate a sufficient contact area (strong interaction) among the neighboring rGO sheets and thereby lead to the pull outs of rGO sheets during the fracture under tensile deformation.

Figure 4d–g shows the mechanical and electrical properties of our graphene fibers depending on the size fractionation of GO sheets. All of the stress–strain curves obtained by tensile tests show typical nonlinear brittle fracture behaviors arising from the highly aligned graphene sheets (Figure 4d). The evolution of tensile modulus and strength is summarized in Figure 4e,f with standard deviations. The tensile strengths of the fibers spun from F1, F2, and F3 of MGO were measured to be 336, 285, and 85 MPa, respectively, revealing a monotonic decreasing tendency with the fractionation order (Figure 4f). The tensile modulus shows a similar tendency with the measurement values of 46, 45, and 23 GPa, respectively (Figure 4d). Note that F1 and F2 have relatively higher moduli compared to F3. Since the initial modulus is generally governed by the interaction strength among the constituting basic particles in the original undeformed state (resist to an external deformation), the rapid decay of modulus in F3 is obviously due to the relatively weak interaction among the small-size rGO sheets. The rGO sheet size is also critical for the elongation at break for the mechanical behavior. Large-sized sheets can accommodate relatively large deformation particularly together with the later sliding among tightly interacting neighboring sheets, which eventually results in the pull-outs of rGO sheets in the fractured surfaces. By contrast, small-size sheets easily lose intersheet interaction even under a relatively small deformation. Taken together, the presence of large-size sheets is found to be critical for high mechanical strength as well as modulus in graphene fibers, while small-size sheets can intercalate the voids and defects inevitably accompanied by the distortion of large sheets.[21,46–48]

The electrical conductivity of the graphene fibers was also measured along the fiber axis direction employing two-point probe method. The conductivity also reveals a proportional relationship with the lateral size of GO, as large-size sheets simply reduces the number of intersheet junctions for the same length of conductive body. The electrical conductivity was measured to be 3.9×10^4, 3.1×10^4, and 2.5×10^4 S/m along the fiber axis direction for F1, F2, and F3, respectively (Figure 4g).

CONCLUSIONS

We have demonstrated a systematic size fractionation over the entire size range of typical polydisperse GO samples by FlFFF. While four different sizes of GO samples prepared by common synthetic protocols were successfully size separated via FlFFF, size criteria for the separation mechanism between the normal mode and the steric/hyperlayer mode were evaluated compared to conventional spherical standards. Liquid crystallinity of the stable GO dispersions was well-identified regardless of the lateral size range and exploited for the facile wet-spinning of graphene fibers under the ambient conditions to confirm the GO size effect on the physical and electrical properties of the resultant fibers. This reliable size separation strategy exploiting FlFFF is generally useful for other 2D materials, such as rGO, transition-metal dichalcogenide (TMD), MXene, black phosphorus (BP), and hexagonal boron nitride (hBN), whose lateral size distribution is crucial for the desired material properties.

METHODS

Materials and Reagents. Polystyrene (PS) latex standards with the nominal diameters of 23 nm, 46 nm, 100 nm, 203 nm, 1.999 μm, 6.007 μm, 10.15 μm, and 19.99 μm were purchased from Thermo Fisher Scientific (Waltham, MA). FL-70 and sodium dodecyl sulfate (SDS) were purchased from Fisher Scientific (Fair Lawn, NJ), and ammonium bicarbonate was purchased from Sigma-Aldrich.

Preparation of GO. GO sheets were prepared by a modified Hummers method from two different graphite sources: MGR 25998k-5 from Graphit Kropfmüch GmbH (Herzenberg, Germany) for MGO and graphite flakes from Sigma-Aldrich (St. Louis, MO) for LGO. SGO was prepared by a 1 h bath sonication using MGO. XSGO was prepared by the horn ultrasonication (Fisher Scientific, Sonic Dismembrator model 500) of MGO with sonication power at 20 W for 1 h in an ice bath.

Flow Field-Flow Fractionation. The channel type utilized for FlFFF was a model LC asymmetrical channel (Wyatt Technology Europe GmbH, Dernbach, Germany) with a regenerated cellulose membrane having a 10000 Da molecular weight cutoff (MWCO) (Merck Millipore, Darmstadt, Germany). The semiprep AF4 channel spacer was made from Mylar sheets, and the thickness of the spacer was 250 μm for XSGO and 350 μm for SGO, MGO, and LGO fractionation. The channel spacer had trapezoidal shapes with an inlet to outlet total length of 26.5 cm for XSGO, SGO and 26.7 cm for MGO, LGO, the width of the inlet part was 2.1 cm for XSGO, SGO, and 4.4 cm for MGO, LGO, and the width of the outlet part was 0.5 cm. The length of each inlet and outlet triangular part was 2.0 and 0.6 cm for XSGO, SGO, and 3.7 and 0.5 for MGO, LGO, respectively. Carrier solutions were prepared with deionized water (>18 MΩ·cm) using three different types of surfactants and chemicals: 0.10% FL-70

https://doi.org/10.1021/acsnano.2c01402
ACS Nano 2022, 16, 9172–9182

or 0.05% SDS, both of which were added with 0.02% NaN_3 as a bactericide for analytical channel, and 3 mM ammonium bicarbonate for semipreparative channel. Each carrier solution was filtered using a nitrocellulose filter (pore size of 0.22 μm, Merck Millipore) prior to use. The carrier solution was delivered to the FlFFF channel using a model SP930D HPLC pump (Young Lin Instruments, Seoul, Korea). Eluted GO sheets were monitored with a UV detector using a wavelength of 254 nm (YL9120 UV from Young-Lin). Sample injection was conducted by using a Model 7125 injector from Rheodyne (Cotati, CA) with a sample loop (30 μL for XSGO, SGO and 50 μL for MGO, LGO) during the focusing/relaxation step. In analytical channel, the injection amounts of MGO and LGO were 16.5 and 6 μg, respectively. For the semipreparative channel, the injection amounts of MGO and LGO were 100 and 115 μg, respectively. Sample materials after injection were focused at a position around 1/10 for XSGO, SGO and 1/9 for MGO, LGO of the channel length by using two counter directing flow streams from both inlet and outlet of the channel. Focusing/relaxation time was 3 min for PS latex standards and 5 min for GO sheet samples using a total flow rate of 3.0 mL/min. Right after the relaxation/focusing procedure, flow was solely directed to the channel inlet to initiate the particle migration. After each run, channel membrane was washed at an outflow rate of 3 mL/min at least 5 min without crossflow. Upon separation, the sample recovery values were calculated by the peak area of MGO sample under a crossflow rate and normalized by the peak area obtained without applying field strength. The calculated recovery value is 78.4% for runs with ammonium bicarbonate solution condition for semipreparative channel.

Characterization of GO. The GO size and morphology of graphene fibers were confirmed by SEM (Hitachi S-4800). The average area of each GO sheet was measured using ImageJ software. The thickness of the GO sheet was analyzed with AFM measurement using NX-10 (Park Systems). Chemical compositions of MGO and size-fractionated MGO were measured with XPS (Theremo VG Scientific, Sigma Probe) and subsequently analyzed by Avantage software. Raman spectra were obtained by ARAMIS (Horiba Jobin Yvon, France) with a 514 nm excitation laser. Mechanical properties of graphene fibers were measured using universal testing machine (UTM, Textechno FAVIMAT+, Germany). The resonance frequency of a fiber (gauge length: 10 mm) was measured while increasing pretension from 0.05 cN with an increment rate of 0.05 cN. The measure tension values as a function of strain were converted based on stress−strain curves. Electrical conductivity of graphene fiber was obtained by two-point prove configuration system (HIOKI, Card HiTester).

Fabrication of Graphene Fiber. Highly concentrated aqueous GO dispersions were transferred to an injection syringe. A coagulation bath was prepared with 5 wt % of $CaCl_2$ dissolved in deionized (DI) water positioned on a parallel rotating disk rotating at a speed of 17 rpm. GO dispersion in the syringe was extruded into this rotating coagulation bath at a flow rate of 0.12 mL min^{-1} using a nozzle with an inner diameter of 500 μm. The end of the spinneret was positioned 3 cm away from the rotating bath center in order to achieve a 1.3 draw ratio. The excessive ions during the coagulation step were removed by immersion into a DI water bath. The washed GO hydrogel fiber was dried at room temperature over 24 h with both fiber ends fixed. For the reduction step, the collected GOLC fibers were located in a quartz tube and placed in a vacuum furnace at a pressure of 3.4×10^5 Torr. Before thermal reduction, the fibers were flushed under the 100 sccm of H_2 stream for 30 min to remove moisture and air absorbed in the fibers. Subsequently, the quartz tube was heated up to 1000 °C at a heating rate of 2 °C min^{-1} under the continuous stream of H_2 gas and held for 2 h. Finally, reduced GF was obtained after cooling to room temperature.[6]

THEORETICAL CONSIDERATIONS

I. General Retention Theory of Flow Field-Flow Fractionation. In FlFFF, the retention ratio, R, is defined as the ratio of void time (t^0) to the retention time (t_r). In the normal mode of FlFFF, R is defined by

$$R = \frac{t^0}{t_r} \cong 6\lambda = \frac{6D}{w^2}\frac{V^0}{\dot{V}_c}\left(D = \frac{kT}{3\pi\eta d_s}\right) \quad (1)$$

where λ (= l/w) is the ratio of mean layer thickness (l) of the sample zone to the channel thickness (w), V^0 is the chanel void volume, and $\dot{V}_c$ is the cross-flow rate at the channel wall. D is the diffusion coefficient of the sample component (= $kT/3\pi\eta d_s$), k is the Boltzmann constant, T is the temperature, η is the viscosity of carrier solution, and d_s is the Stokes′ diameter (or the hydrodynamic diamneter).[31]

However, the retention ratio in the steric/hyperlayer mode is expressed as

$$R = \frac{t^0}{t_r} = \frac{3\gamma d_s}{w} \quad (2)$$

where γ is the steric correction factor, which depends on the field strength, migration flow velocity, and particle diameter.[58] Therefore, the retention ratio can be written as the sum of eqs 1 and 2 like

$$R = \frac{t^0}{t_r} = 6\lambda + \frac{3\gamma d}{w} \quad (3)$$

II. Particle Shape Effect on Retention Ratio. Even if the same diameter of 2D GO and three-dimensional (3D) PS latex bead is used, the elution behavior of 2D GO in the FFF channel is different from that of the 3D PS latex bead in our experiments. Furthermore, the steric transition diameter of 2D GOs is larger than that of PS latex beads. These results originate from the particle shape effect on the retention behavior in the FFF channel. Generally, the 2D GO preserves a nearly flat (self-avoiding) conformation in an aqueous solution.[59] To verify the retention behavior of 2D GO, the particle shape effect on the retention was investigated by the simplest shaped models with disc particles, as suggested by Beckett and Giddings.[40]

In normal mode, the retention ratio of spherical PS beads is 6λ when $l \ll w$. Due to the steric-entropic effect, however, the retention ratio of disc particles was derived as 18λ when $a/l \rightarrow \infty$, where a is the particle radius. The steric-entropic effect examined here is based on an entropic restriction of disc particles as they approach within a distance of the accumulation wall. This loss of entropy of disc particles can cause an increase in mean cloud thickness l compared with spheres of the same mass. Thus, the retention time would be reduced and the retention ratio increased. These results can be interpreted by the shape effect results of 2D GO in normal mode. For more details about steric effects for nonspherical particles, see the previous papers.[40,60]

In the steric/hyperlayer mode, the retention ratio is proportional to the 3γ. The steric correction factor, γ, is affected by many factors, including experimental conditions (field strength, migration flow velocity), particle size, and shape. Until now, there have been no accurate relationships between them. However, the particle's shape absolutely affects the retention ratio in the steric/hyperlayer mode.

It is well-known that the steric transition diameter of the spherical particle is nearly 1 μm or less.[31,61] Here, we have verified that the size of steric conversion of 2D GO is around 3 μm. Furthermore, we demonstrated that the elution of 2D GO

https://doi.org/10.1021/acsnano.2c01402
ACS Nano 2022, 16, 9172−9182

appeared to be faster than that of the spherical PS latex bead in both the normal and steric/hyperlayer mode. As discussed here, the main reason arose from its original 2D planner shape, which causes the different elution behavior from the PS latex bead. Thus, a PS bead and 2D GO with identical diameters have different retention in the FlFFF. These results could apply to other 2D materials that can be dispersed in the solvent, such as MXene, transition-metal dichalcogenide (TMD), etc., to size separation/analysis by FlFFF.

ASSOCIATED CONTENT

Supporting Information

The Supporting Information is available free of charge at https://pubs.acs.org/doi/10.1021/acsnano.2c01402.

Photograph of FlFFF system; working mass range of size separation techniques and size distribution of GO; photograph and size distribution of as-synthesized LGO and SGO; AFM characterization; detailed information on size measurements method; fractogram and size distribution of MGO; fractogram and size distribution of XSGO; fractogram and size distribution of SGO; fractogram of LGO (PDF)

AUTHOR INFORMATION

Corresponding Authors

Myeong Hee Moon − *Department of Chemistry, Yonsei University, Seoul 03722, Republic of Korea;* orcid.org/0000-0002-5454-2601; Email: mhmoon@yonsei.ac.kr

Sang Ouk Kim − *National Creative Research Initiative Center for Multi-Dimensional Directed Nanoscale Assembly, Department of Materials Science and Engineering, Korea Advanced Institute of Science and Technology (KAIST), Daejeon 34141, Republic of Korea;* orcid.org/0000-0003-1513-6042; Email: sangouk.kim@kaist.ac.kr

Authors

Hee Jae Choi − *National Creative Research Initiative Center for Multi-Dimensional Directed Nanoscale Assembly, Department of Materials Science and Engineering, Korea Advanced Institute of Science and Technology (KAIST), Daejeon 34141, Republic of Korea*

Myoungjae Ko − *Department of Chemistry, Yonsei University, Seoul 03722, Republic of Korea*

In Ho Kim − *National Creative Research Initiative Center for Multi-Dimensional Directed Nanoscale Assembly, Department of Materials Science and Engineering, Korea Advanced Institute of Science and Technology (KAIST), Daejeon 34141, Republic of Korea*

Hayoung Yu − *Institute of Advanced Composite Materials, Korea Institute of Science and Technology (KIST), Jeonrabuk-do 55324, Republic of Korea*

Jin Yong Kim − *Department of Chemistry, Yonsei University, Seoul 03722, Republic of Korea*

Taeyeong Yun − *National Creative Research Initiative Center for Multi-Dimensional Directed Nanoscale Assembly, Department of Materials Science and Engineering, Korea Advanced Institute of Science and Technology (KAIST), Daejeon 34141, Republic of Korea*

Joon Seon Yang − *Department of Chemistry, Yonsei University, Seoul 03722, Republic of Korea*

Geon Gug Yang − *National Creative Research Initiative Center for Multi-Dimensional Directed Nanoscale Assembly, Department of Materials Science and Engineering, Korea Advanced Institute of Science and Technology (KAIST), Daejeon 34141, Republic of Korea*

Hyeon Su Jeong − *Institute of Advanced Composite Materials, Korea Institute of Science and Technology (KIST), Jeonrabuk-do 55324, Republic of Korea;* orcid.org/0000-0003-0958-8173

Complete contact information is available at: https://pubs.acs.org/10.1021/acsnano.2c01402

Author Contributions

⊥H.J.C. and M.K. contributed equally to this work.

Notes

The authors declare no competing financial interest.

ACKNOWLEDGMENTS

This work was supported by the Multi-Dimensional Directed Nanoscale Assembly Creative Research Initiative (CRI) Center (2015R1A3A2033061), the Hybrid Interface Materials Research Group (Global Frontier Project, 2013M3A6B1078874), and Grant No. NRF-2021R1A2C2003171 from the National Research Foundation (NRF) of Korea.

REFERENCES

(1) Paredes, J. I.; Villar-Rodil, S.; Martinez-Alonso, A.; Tascón, J. M. D. Graphene Oxide Dispersions in Organic Solvents. *Langmuir* **2008**, *24*, 10560−10564.

(2) Konios, D.; Stylianakis, M. M.; Stratakis, E.; Kymakis, E. Dispersion Behaviour of Graphene Oxide and Reduced Graphene Oxide. *J. Colloid Interface Sci.* **2014**, *430*, 108−112.

(3) Bullock, C. J.; Bussy, C. Biocompatibility Considerations in the Design of Graphene Biomedical Materials. *Adv. Mater. Interfaces* **2019**, 1900229.

(4) Gao, W.; Alemany, L. B.; Ci, L. J.; Ajayan, P. M. New Insights into the Structure and Reduction of Graphite Oxide. *Nat. Chem.* **2009**, *1*, 403−408.

(5) Park, Y.; Shim, J.; Jeong, S.; Yi, G. R.; Chae, H.; Bae, J. W.; Kim, S. O.; Pang, C. Microtopography-Guided Conductive Patterns of Liquid-Driven Graphene Nanoplatelet Networks for Stretchable and Skin-Conformal Sensor Array. *Adv. Mater.* **2017**, *29*, 1606453.

(6) Kim, I. H.; Yun, T.; Kim, J. E.; Yu, H.; Sasikala, S. P.; Lee, K. E.; Koo, S. H.; Hwang, H.; Jung, H. J.; Park, J. Y.; Jeong, H. S.; Kim, S. O. Mussel-Inspired Defect Engineering of Graphene Liquid Crystalline Fibers for Synergistic Enhancement of Mechanical Strength and Electrical Conductivity. *Adv. Mater.* **2018**, *30*, 1803267.

(7) Abraham, J.; Vasu, K.; Williams, C.; Gopinadhan, K.; Su, Y.; Cherian, C.; Dix, J.; Prestat, E.; Haigh, S.; Grigorieva, I.; Carbone, P.; Geim, A. K.; Nair, R. R. Tunable Sieving of Ions Using Graphene Oxide Membranes. *Nat. Nanotechnol.* **2017**, *12*, 546−550.

(8) Nie, L.; Goh, K.; Wang, Y.; Lee, J.; Huang, Y.; Karahan, H. E.; Zhou, K.; Guiver, M. D.; Bae, T. H. Realizing Small-Flake Graphene Oxide Membranes for Ultrafast Size-Dependent Organic Solvent Nanofiltration. *Sci. Adv.* **2020**, *6*, eaaz9184.

(9) Chen, H.; Yang, Y. F.; Boyle, D. T.; Jeong, Y. K.; Xu, R.; de Vasconcelos, L. S.; Huang, Z. J.; Wang, H. S.; Wang, H. X.; Huang, W. X.; Li, H. Q.; Wang, J. Y.; Gu, H. K.; Matsumoto, R.; Motohashi, K.; Nakayama, Y.; Zhao, K. J.; Cui, Y. Free-Standing Ultrathin Lithium Metal-Graphene Oxide Host Foils with Controllable Thickness for Lithium Batteries. *Nat. Energy* **2021**, *6*, 790−798.

(10) Park, H.; Lee, K.; Kim, Y.; Ambade, S.; Noh, S.; Eom, W.; Hwang, J.; Lee, W.; Huang, J.; Han, T. H. Dynamic Assembly of Liquid Crystalline Graphene Oxide Gel Fibers for Ion Transport. *Sci. Adv.* **2018**, *4*, eaau2104.

(11) Geng, H. Y.; Yao, B. W.; Zhou, J. J.; Liu, K.; Bai, G. Y.; Li, W. B.; Song, Y. L.; Shi, G. Q.; Doi, M.; Wang, J. J. Size Fractionation of

Graphene Oxide Nanosheets *via* Controlled Directional Freezing. *J. Am. Chem. Soc.* **2017**, *139*, 12517−12523.
(12) Lee, K. E.; Kim, J. E.; Maiti, U. N.; Lim, J.; Hwang, J. O.; Shim, J.; Oh, J. J.; Yun, T.; Kim, S. O. Liquid Crystal Size Selection of Large-Size Graphene Oxide for Size-Dependent N-Doping and Oxygen Reduction Catalysis. *ACS Nano* **2014**, *8*, 9073−9080.
(13) Kim, J. E.; Han, T. H.; Lee, S. H.; Kim, J. Y.; Ahn, C. W.; Yun, J. M.; Kim, S. O. Graphene Oxide Liquid Crystals. *Angew. Chem., Int. Ed.* **2011**, *50*, 3043−3047.
(14) Padmajan Sasikala, S.; Lim, J.; Kim, I. H.; Jung, H. J.; Yun, T.; Han, T. H.; Kim, S. O. Graphene Oxide Liquid Crystals: A Frontier 2D Soft Material for Graphene-Based Functional Materials. *Chem. Soc. Rev.* **2018**, *47*, 6013−6045.
(15) Hummers, W. S., Jr.; Offeman, R. E. Preparation of Graphene Oxide. *J. Am. Chem. Soc.* **1958**, *80*, 1339.
(16) Pei, S. F.; Wei, Q. W.; Huang, K.; Cheng, H. M.; Ren, W. C. Green Synthesis of Graphene Oxide by Seconds Timescale Water Electrolytic Oxidation. *Nat. Commun.* **2018**, *9*, 145.
(17) Dimiev, A. M.; Tour, J. M. Mechanism of Graphene Oxide Formation. *ACS Nano* **2014**, *8*, 3060−3068.
(18) Zhang, L.; Liang, J.; Huang, Y.; Ma, Y.; Wang, Y.; Chen, Y. Size-Controlled Synthesis of Graphene Oxide Sheets on A Large Scale Using Chemical Exfoliation. *Carbon* **2009**, *47*, 3365−3368.
(19) Zhao, J. P.; Pei, S. F.; Ren, W. C.; Gao, L. B.; Cheng, H. M. Efficient Preparation of Large-Area Graphene Oxide Sheets for Transparent Conductive Films. *ACS Nano* **2010**, *4*, 5245−5252.
(20) Kumar, P.; Shahzad, F.; Yu, S.; Hong, S. M.; Kim, Y. H.; Koo, C. M. Large-Area Reduced Graphene Oxide Thin Film with Excellent Thermal Conductivity and Electromagnetic Interference Shielding Effectiveness. *Carbon* **2015**, *94*, 494−500.
(21) Xu, Z.; Sun, H. Y.; Zhao, X. L.; Gao, C. Ultrastrong Fibers Assembled from Giant Graphene Oxide Sheets. *Adv. Mater.* **2013**, *25*, 188−193.
(22) Perreault, F.; de Faria, A. F.; Nejati, S.; Elimelech, M. Antimicrobial Properties of Graphene Oxide Nanosheets: Why Size Matters. *ACS Nano* **2015**, *9*, 7226−7236.
(23) Szabo, T.; Maroni, P.; Szilagyi, I. Size-Dependent Aggregation of Graphene Oxide. *Carbon* **2020**, *160*, 145−155.
(24) Kim, J.; Cote, L. J.; Huang, J. X. Two Dimensional Soft Material: New Faces of Graphene Oxide. *Acc. Chem. Res.* **2012**, *45*, 1356−1364.
(25) Chen, J.; Li, Y. R.; Huang, L.; Jia, N.; Li, C.; Shi, G. Q. Size Fractionation of Graphene Oxide Sheets *via* Filtration through Track-Etched Membranes. *Adv. Mater.* **2015**, *27*, 3654−3660.
(26) Wang, X. L.; Bai, H.; Shi, G. Q. Size Fractionation of Graphene Oxide Sheets by pH-Assisted Selective Sedimentation. *J. Am. Chem. Soc.* **2011**, *133*, 6338−6342.
(27) Sun, X. M.; Luo, D. C.; Liu, J. F.; Evans, D. G. Monodisperse Chemically Modified Graphene Obtained by Density Gradient Ultracentrifugal Rate Separation. *ACS Nano* **2010**, *4*, 3381−3389.
(28) Williams, S. K. R.; Runyon, J. R.; Ashames, A. A. Field-Flow Fractionation: Addressing the Nano Challenge. *Anal. Chem.* **2011**, *83*, 634−642.
(29) Viebke, C.; Williams, P. A. The Influence of Temperature on the Characterization of Water-Soluble Polymers Using Asymmetric Flow Field-Flow-Fractionation Coupled to Multiangle Laser Light Scattering. *Anal. Chem.* **2000**, *72*, 3896−3901.
(30) Tan, Z. Q.; Liu, J. F.; Guo, X. R.; Yin, Y. G.; Byeon, S. K.; Moon, M. H.; Jiang, G. B. Toward Full Spectrum Speciation of Silver Nanoparticles and Ionic Silver by On-Line Coupling of Hollow Fiber Flow Field-Flow Fractionation and Minicolumn Concentration with Multiple Detectors. *Anal. Chem.* **2015**, *87*, 8441−8447.
(31) Kowalkowski, T.; Sugajski, M.; Buszewski, B. Impact of Ionic Strength of Carrier Liquid on Recovery in Flow Field-Flow Fractionation. *Chromatographia* **2018**, *81*, 1213−1218.
(32) Kim, Y. B.; Yang, J. S.; Moon, M. H. Investigation of Steric Transition with Field Programming in Frit Inlet Asymmetrical Flow Field-Flow Fractionation. *J. Chromatogr. A* **2018**, *1576*, 131−136.
(33) Kowalkowski, T.; Buszewski, B.; Cantado, C.; Dondi, F. Field-Flow Fractionation: Theory, Techniques, Applications and the Challenges. *Crit. Rev. Anal. Chem.* **2006**, *36*, 129−135.
(34) Ratanathanawongs, S. K.; Lee, I.; Giddings, J. C. Separation and Characterization of 0.01−50-Mu-M Particles Using Flow Field-Flow Fractionation. *ACS Sym. Ser.* **1991**, *472*, 229−246.
(35) Giddings, J. C. Field-Flow Fractionation - Analysis of Macromolecular, Colloidal, and Particulate Materials. *Science* **1993**, *260*, 1456−1465.
(36) Contado, C. Field Flow Fractionation Techniques to Explore the "Nano-World". *Anal. Bioanal. Chem.* **2017**, *409*, 2501−2518.
(37) Malik, M. I.; Pasch, H. Field-Flow Fractionation: New and Exciting Perspectives in Polymer Analysis. *Prog. Polym. Sci.* **2016**, *63*, 42−85.
(38) Moon, M. H.; Lee, K. H.; Min, B. R. Effect of Temperature on Particle Separation in Hollow Fiber Flow Field-Flow Fractionation. *J. Microcolumn. Sep.* **1999**, *11*, 676−681.
(39) Eskelin, K.; Oksanen, H. M.; Poranen, M. M. Sample Carryover and Cleaning Procedures for Asymmetrical Flow Field-Flow Fractionation Instrument. *J. Chromatogr. B* **2021**, *1181*, 122920.
(40) Beckett, R.; Giddings, J. C. Entropic Contribution to the Retention of Nonspherical Particles in Field-Flow Fractionation. *J. Colloid Interface Sci.* **1997**, *186*, 53−59.
(41) Schimpf, M. E.; Caldwell, K.; Giddings, J. C. *Field-Flow Fractionation Handbook*; Wiley-Interscience: New York, 2000.
(42) Peterson, R. E.; Myers, M. N.; Giddings, J. C. Characterization of Steric Field-Flow Fractionation Using Particles to 100 μm Diameter. *Sep. Sci. Technol.* **1984**, *19*, 307−319.
(43) Stoller, M. D.; Park, S. J.; Zhu, Y. W.; An, J. H.; Ruoff, R. S. Graphene-Based Ultracapacitors. *Nano Lett.* **2008**, *8*, 3498−3502.
(44) Chabot, V.; Higgins, D.; Yu, A. P.; Xiao, X. C.; Chen, Z. W.; Zhang, J. J. A Review of Graphene and Graphene Oxide Sponge: Material Synthesis and Applications to Energy and the Environment. *Energy Environ. Sci.* **2014**, *7*, 1564−1596.
(45) Liu, X.; Liu, D.; Lee, J. H.; Zheng, Q. B.; Du, X. H.; Zhang, X. Y.; Xu, H. R.; Wang, Z. Y.; Wu, Y.; Shen, X.; Cui, J.; Ma, Y. W.; Kim, J. K. Spider-Web-Inspired Stretchable Graphene Woven Fabric for Highly Sensitive, Transparent, Wearable Strain Sensors. *ACS Appl. Mater. Interfaces* **2019**, *11*, 2282−2294.
(46) Xin, G. Q.; Yao, T. K.; Sun, H. T.; Scott, S. M.; Shao, D. L.; Wang, G. K.; Lian, J. Highly Thermally Conductive and Mechanically Strong Graphene Fibers. *Science* **2015**, *349*, 1083−1087.
(47) Xu, Z.; Gao, C. Graphene Fiber: A New Trend in Carbon Fibers. *Mater. Today* **2015**, *18*, 480−492.
(48) Dong, L.; Yang, J.; Chhowalla, M.; Loh, K. P. Synthesis and Reduction of Large Sized Graphene Oxide Sheets. *Chem. Soc. Rev.* **2017**, *46*, 7306−7316.
(49) Pan, S. Y.; Aksay, I. A. Factors Controlling the Size of Graphene Oxide Sheets Produced *via* the Graphite Oxide Route. *ACS Nano* **2011**, *5*, 4073−4083.
(50) Shao, G. L.; Lu, Y. G.; Wu, F. F.; Yang, C. L.; Zeng, F. L.; Wu, Q. L. Graphene Oxide: The Mechanisms of Oxidation and Exfoliation. *J. Mater. Sci.* **2012**, *47*, 4400−4409.
(51) Luo, J. Y.; Cote, L. J.; Tung, V. C.; Tan, A. T. L.; Goins, P. E.; Wu, J. S.; Huang, J. X. Graphene Oxide Nanocolloids. *J. Am. Chem. Soc.* **2010**, *132* (50), 17667−17669.
(52) Szabo, T.; Berkesi, O.; Forgo, P.; Josepovits, K.; Sanakis, Y.; Petridis, D.; Dekany, I. Evolution of Surface Functional Groups in A Series of Progressively Oxidized Graphite Oxides. *Chem. Mater.* **2006**, *18* (11), 2740−2749.
(53) Lerf, A.; He, H. Y.; Forster, M.; Klinowski, J. Structure of Graphite Oxide Revisited. *J. Phys. Chem. B* **1998**, *102*, 4477−4482.
(54) Eigler, S.; Dotzer, C.; Hirsch, A. Visualization of Defect Densities in Reduced Graphene Oxide. *Carbon* **2012**, *50*, 3666−3673.
(55) Jeong, S. Y.; Kim, S. H.; Han, J. T.; Jeong, H. J.; Yang, S.; Lee, G. W. High-Performance Transparent Conductive Films Using Rheologically Derived Reduced Graphene Oxide. *ACS Nano* **2011**, *5*, 870−878.

https://doi.org/10.1021/acsnano.2c01402
ACS Nano 2022, 16, 9172−9182

(56) Kim, I. H.; Im, T. H.; Lee, H. E.; Jang, J. S.; Wang, H. S.; Lee, G. Y.; Kim, I. D.; Lee, K. J.; Kim, S. O. Janus Graphene Liquid Crystalline Fiber with Tunable Properties Enabled by Ultrafast Flash Reduction. *Small* **2019**, *15*, 1901529.
(57) Liu, Y.; Xie, B.; Zhang, Z.; Zheng, Q.; Xu, Z. Mechanical properties of graphene papers. *J. Mech. Phys. Solids* **2012**, *60*, 591−605.
(58) Myers, M. N.; Giddings, J. C. Properties of the Transition from Normal to Steric Field-Flow Fractionation. *Anal. Chem.* **1982**, *54*, 2284−2289.
(59) Li, P.; Wang, S. J.; Meng, F. X.; Wang, Y.; Guo, F.; Rajendran, S.; Gao, C.; Xu, Z. P.; Xu, Z. Conformational Scaling Relations of Two-Dimensional Macromolecular Graphene Oxide in Solution. *Macromolecules* **2020**, *53*, 10421−10430.
(60) Phelan, F. R.; Bauer, B. J. Comparison of steric effects in the modeling of spheres and rodlike particles in field-flow fractionation. *Chem. Eng. Sci.* **2009**, *64*, 1747−1758.
(61) Jensen, K. D.; Williams, S. R.; Giddings, J. C. High-speed particle separation and steric inversion in thin flow field-flow fractionation channels. *J. Chromatogr. A* **1996**, *746*, 137−145.

https://doi.org/10.1021/acsnano.2c01402
ACS Nano 2022, 16, 9172−9182